

Figure 4 Top panel, threshold voltage at 20 K, $V_{\text{threshold}}$, from a high-resistivity (HR) to a low-resistivity (LR) state, plotted as a function of magnetic field (see Fig. 3). Bottom panel, magnetoelectronic phase diagram of $\text{Pr}_{1-x}\text{Ca}_x\text{MnO}_3$ ($x = 0.3$) as a function of magnetic field. Two phase boundaries were determined by field-scan at a fixed temperature. Open circles, critical fields from the charge-ordered insulating (COI) to ferromagnetic metallic (FM) state; filled circles, critical fields for the reverse transition. In the COI state, Mn^{3+} and Mn^{4+} species are regularly ordered on the crystal lattice, while the average valence of Mn ion is $3.3+$ in the FM state, as shown in the schematics. The hatched region represents hysteresis where both the COI and FM states are realized, depending on the experimental history on the phase diagram. Experimental conditions of Fig. 3 are indicated by filled triangles.

should immediately lead to the appearance of a metallic state accompanied by a large number of mobile charge carriers (or by a large Fermi surface), and hence is intrinsically different from conventional semiconductors or band insulators. The current-switching phenomenon may be used for the fabrication of electromagnets on a micrometre or nanometre scale, as the switching between the low-resistivity and high-resistivity states in the manganites with charge-ordered instabilities is expected to be accompanied by a metamagnetic transition. This may open the way to a variety of applications such as STM-tip-assisted nanofabrication of ferromagnetic domains in antiferromagnetic matrices. □

Received 27 November 1996; accepted 21 May 1997.

- Baibich, M. N. *et al.* Giant magnetoresistance of (001)Fe/(001)Cr magnetic superlattices. *Phys. Rev. Lett.* **61**, 2472–2475 (1988).
- Kusters, R. M., Singleton, D. A., Mcgreevy, R. & Hayes, W. Magnetoresistance measurements on the magnetic semiconductor $\text{Nd}_{0.5}\text{Pb}_{0.5}\text{MnO}_3$. *Physica B* **155**, 362–365 (1989).
- von Helmlert, R., Wecker, J., Holzapfel, B., Schultz, M. & Samwer, K. Giant negative magnetoresistance in perovskite $\text{La}_{2/3}\text{Ba}_{1/3}\text{MnO}_3$ ferromagnetic films. *Phys. Rev. Lett.* **71**, 2331–2333 (1993).
- Jin, S. *et al.* Thousandfold change in resistivity in magnetoresistive La-Ca-Mn-O films. *Science* **264**, 413–415 (1994).
- Tokura, Y. *et al.* Giant magnetotransport phenomena in filling-controlled Kondo lattice system: $\text{La}_{1-x}\text{Sr}_x\text{MnO}_3$. *J. Phys. Soc. Jpn* **63**, 3931–3935 (1994).
- Urushibara, A. *et al.* Insulator-metal transition and giant magnetoresistance in $\text{La}_{1-x}\text{Sr}_x\text{MnO}_3$. *Phys. Rev. B* **51**, 11103–11109 (1995).
- Tomioka, Y., Asamitsu, A., Moritomo, Y., Kuwahara, H. & Tokura, Y. Collapse of a charge-ordered state under a magnetic field in $\text{Pr}_{1/2}\text{Sr}_{1/2}\text{MnO}_3$. *Phys. Rev. Lett.* **74**, 5108–5111 (1995).
- Tomioka, Y., Asamitsu, A., Moritomo, Y. & Tokura, Y. Anomalous magnetotransport properties of $\text{Pr}_{1-x}\text{Ca}_x\text{MnO}_3$. *J. Phys. Soc. Jpn* **64**, 3626–3630 (1995).
- Tomioka, Y., Asamitsu, A., Kuwahara, H., Moritomo, Y. & Tokura, Y. Magnetic-field-induced metal-insulator phenomena in $\text{Pr}_{1-x}\text{Ca}_x\text{MnO}_3$ with controlled charge-ordering instability. *Phys. Rev. B* **53**, R1689–R1692 (1995).

- Kuwahara, H., Tomioka, Y., Asamitsu, A., Moritomo, Y. & Tokura, Y. A first-order phase transition induced by a magnetic field. *Science* **270**, 961–963 (1995).
- Kuwahara, H. *et al.* Striction-coupled magnetoresistance in perovskite-type manganese oxides. *Science* **272**, 80–82 (1996).
- Jonker, G. H. & Van Santen, J. H. Ferromagnetic compounds of manganese with perovskite structure. *Physica* **16**, 337–349 (1950).
- Zener, C. Interaction between the *d*-shells in the transition metals. II. Ferromagnetic compounds of manganese with perovskite structure. *Phys. Rev.* **82**, 403–405 (1951).
- Anderson, P. W. & Hasegawa, H. Considerations on double exchange. *Phys. Rev.* **100**, 675–681 (1955).
- de Gennes, P.-G. Effects of double exchange in magnetic crystals. *Phys. Rev.* **118**, 141–154 (1960).
- Jirak, Z., Krupicka, S., Simsa, Z., Dlouha, M. & Vratislav, Z. Neutron diffraction study of $\text{Pr}_{1-x}\text{Ca}_x\text{MnO}_3$ perovskite. *J. Magn. Magn. Mater.* **53**, 153–166 (1985).
- Yoshizawa, H., Kawano, H., Tomioka, Y. & Tokura, Y. Neutron-diffraction study of the magnetic-field-induced metal-insulator transition in $\text{Pr}_{0.7}\text{Ca}_{0.3}\text{MnO}_3$. *Phys. Rev. B* **52**, R13145–R13148 (1995).

Acknowledgements. This work was performed at JRCAT under the joint research agreement between the NAIK and the ATP, and was supported by NEDO and by a Grant-In-Aid for Scientific Research from the Ministry of Education, Science, and Culture, Japan.

Correspondence and requests for materials should be addressed to A.A. (e-mail: asamitsu@jrcat.or.jp).

Controlled production of aligned-nanotube bundles

M. Terrones*, N. Grobert*, J. Olivares*, J. P. Zhang†, H. Terrones‡, K. Kordatos*, W. K. Hsu*, J. P. Hare*, P. D. Townsend*, K. Prassides*, A. K. Cheetham†, H. W. Kroto* & D. R. M. Walton*

* School of Chemistry, Physics and Environmental Science, University of Sussex, Brighton BN1 9QJ, UK

† Materials Research Laboratory, University of California, Santa Barbara, California 93106, USA

‡ Instituto de Fisica, UNAM, Apartado Postal 20-364, 01000 México DF, México

Carbon nanotubes^{1,2} might be usefully employed in nanometre-scale engineering and electronics. Electrical conductivity measurements on the bulk material^{3,4}, on individual multi-walled^{5,6} and single-walled⁷ nanotubes and on bundles of single-walled nanotubes^{8,9} have revealed that they may behave as metallic, insulating or semiconducting nanowires, depending on the method of production—which controls the degree of graphitization, the helicity and the diameter. Measurements of Young's modulus show¹⁰ that single nanotubes are stiffer than commercial carbon fibres. Methods commonly used to generate nanotubes—carbon-arc discharge techniques^{1,2,4}, catalytic pyrolysis of hydrocarbons^{11,12} and condensed-phase electrolysis^{13,14}—generally suffer from the drawbacks that polyhedral particles are also formed and that the dimensions of the nanotubes are highly variable. Here we describe a method for generating aligned carbon nanotubes by pyrolysis of 2-amino-4,6-dichloro-*s*-triazine over thin films of a cobalt catalyst patterned on a silica substrate by laser etching. The use of a patterned catalyst apparently encourages the formation of aligned nanotubes. The method offers control over length (up to about 50 μm) and fairly uniform diameters (30–50 nm), as well as producing nanotubes in high yield, uncontaminated by polyhedral particles.

In a typical experiment, a thin film of cobalt (~10–100 nm) was deposited on a silica plate (1 mm thick, 5 mm wide and 20 mm long) using the following technique. A laser beam (Nd:YAG, wavelength 266 nm, 40 mJ per pulse, 10 Hz) was focused (spot size 2 mm outer diameter) on a rotating cobalt target (1.5 cm^2 , 0.25 mm thick) for 10–30 min under vacuum ($\leq 1 \times 10^{-6}$ torr). The silica plate, which was heated to 350 °C during the laser ablation process, was aligned 40 mm from and parallel to the target. Following ablation, the plate was exposed to air and etched with a single laser pulse (5 mJ) using cylindrical lenses (65 mm focal length) to create linear tracks (widths 1–20 μm , lengths ≤ 5 mm; Fig. 1)¹⁶.

A sample of vacuum-dried 2-amino-4,6-dichloro-*s*-triazine (0.02–0.15 g), prepared from cyanuric chloride and ammonia¹⁵, was introduced into one end of a silica tube (6 mm outside

diameter, length 60 cm), and the silica plate coated with etched cobalt was placed face downwards at the other end. The tube was inserted into a two-stage furnace¹⁷ fitted with independent temperature controllers (Fig. 2). Argon gas ($20 \text{ cm}^3 \text{ min}^{-1}$) was passed through the system and the temperature of the second furnace was set at 950°C . The temperature of the first furnace was then raised at $15^\circ\text{C min}^{-1}$ to 200°C and then, by 100°C increments (5 min per increment) to $1,000^\circ\text{C}$. After 5 min at this temperature, the first furnace was allowed to cool to room temperature, but the second furnace was maintained at 950°C for an additional 15 min in order to complete the annealing process. At this stage, the silica plate was covered with dark tracks visible to the naked eye; those areas where the cobalt film had not been laser-etched were transparent (see below).

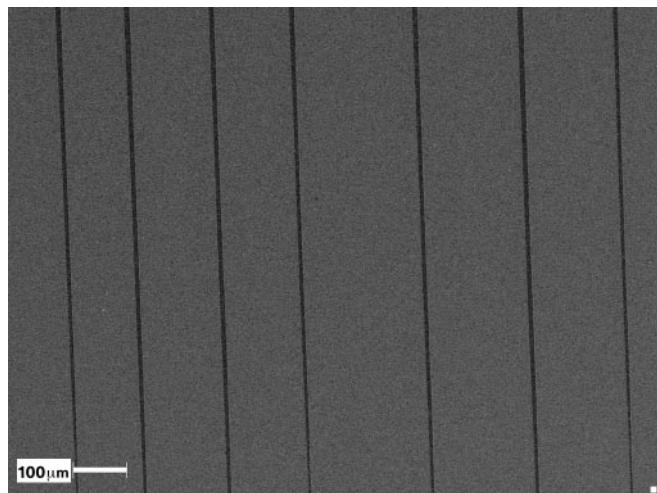


Figure 1 SEM image showing uniform tracks etched by the laser beam. It is believed that along these channels/tracks uniform cobalt nanoparticles are deposited evenly by the laser striking over the thin film. Scale bar, $100 \mu\text{m}$.

A series of silica plates, treated in this way, were coated with gold and examined by scanning electron microscopy, SEM (Leo 5420 operated at 20 keV). The black deposit on a second series of plates was removed by scraping, dispersed in acetone, and analysed by the following techniques: transmission electron microscopy (TEM, using a JEOL JEM 100CX at 100 keV), high resolution TEM (HRTEM, using a JEOL JEM 2010 at 200 keV and a JEM 4000 at 400 keV, and a Gatan GIF system operated at 200 kV with 0.3-eV dispersion for fine structure study) and energy dispersive X-ray analysis, EDX (using a NORAN Instruments detector attached to the latter microscope). Residues from the acetone exit bubblers (Fig. 2) were analysed by mass spectrometry, MS (VG autospec, electron impact, 70 eV).

SEM studies of the gold-coated plates revealed the presence of

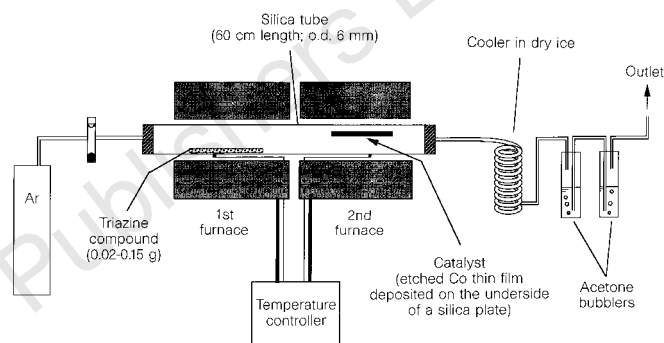
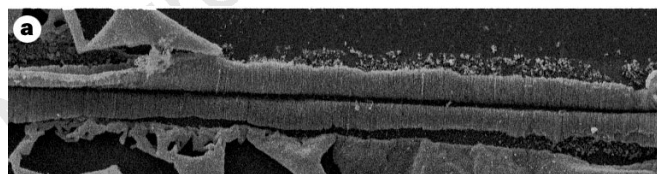
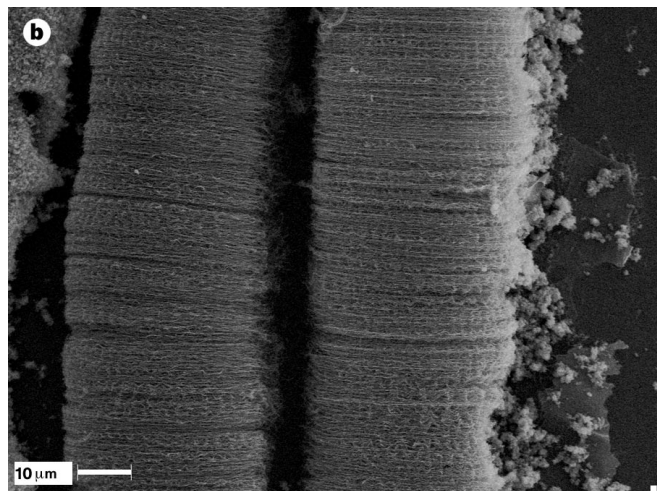


Figure 2 Pyrolysis device, illustrating the two-stage furnace system.

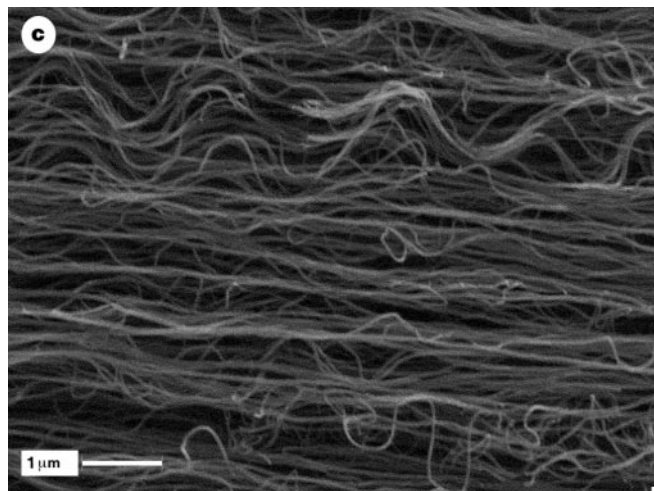


100 μm



10 μm

Figure 3 SEM images of aligned nanotube bundles. **a**, Low-magnification of adjacent bundles in which nanotubes appear aligned. Scale bar, $100 \mu\text{m}$. **b**, **c**, Higher magnification of one bundle, showing aligned nanotubes of uniform length ($40 \mu\text{m}$) and diameter (30–50 nm). Scale bars: in **b**, $10 \mu\text{m}$; in **c**, $1 \mu\text{m}$.



1 μm

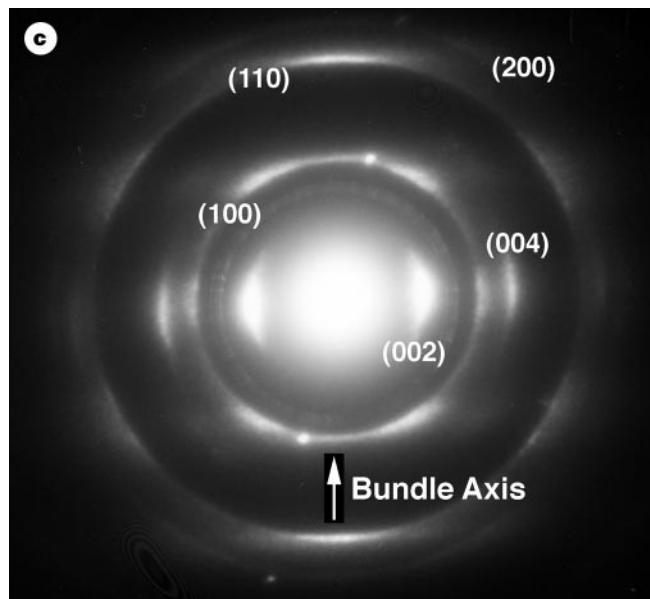
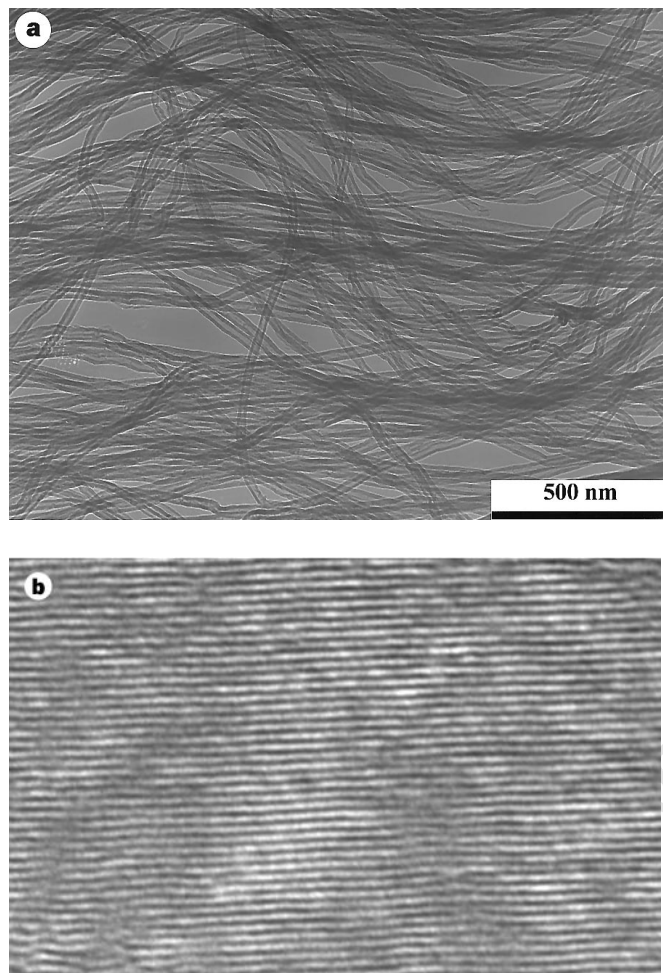


Figure 4 a, TEM image of a typical region filled with pure nanotubes dispersed by sonication. Encapsulated and polyhedral particles or other graphitic nanostructures are absent. Scale bar, 500 nm. **b**, HRTEM image showing good graphitization within the nanotubes (interlayer spacing ~ 3.4 Å). **c**, Electron diffraction pattern from the group of nanotubes, exhibiting a collective feature. The tubes are grown in the direction indicated by the headed arrow. The centre of the first ring corresponds to 3.4 Å in real space, the rings revealing the presence of hexagonal graphite (armchair arrangement) which has an orientational relationship with the nanotubes. The walls of the tubes are parallel to (0001) reflections.

nanotube bundles closely aligned with the nanotracks (length 1–5 mm) created by laser etching. The tubes within these bundles were of uniform length (≤ 50 μm) and external diameter (~ 30 – 50 nm; Fig. 3). The residual cobalt on the plate was removed, probably by the action of HCl, and was collected in the exit bubblers as cobalt chloride. We note that no traces of encapsulated or polyhedral particles were detected. Aligned-nanotube films also were observed in other etched regions.

TEM and HRTEM observations (Fig. 4a, b) confirm the presence of multi-layered graphitic tubules (30–50 nm outer diameter, 60–80 layers). In most cases, cobalt (particles ≤ 50 nm diameter) was detected by EDX analysis within the nanotube tips. These particles appear to be responsible for the nanotube growth, but they were absent from a significant number (5%) of the closed end-caps. Occasionally, substantial sections of tubes were filled with cobalt. Analyses (using electron energy-loss spectroscopy, EELS) show that the nanotubes consist of pure carbon accompanied by traces of nitrogen (< 2 – 5%). Sharp ionization edges at 284 and 291 eV correspond to π^* and σ^* features associated with sp^2 hybridized carbon. A very broad weak feature at 400 eV may be due to nitrogen, generated during triazine decomposition and trapped inside the tubules. Both EELS and EDX measurements indicate that chlorine is entirely absent.

The deposition of a cobalt thin film on silica by laser ablation seems to be an efficient method for producing a uniform distribution of the metal catalyst. Subsequent laser-etching generates tracks or areas free of cobalt (Fig. 1), leaving cobalt particles evenly positioned along the edges of the eroded tracks or stripes¹⁶. These particles (≤ 50 nm), which exhibit a large surface/volume ratio,

appear to be responsible for the carbon agglomeration and the unique nanotube growth behaviour reported here. An important factor in our experiments is the ratio of organic precursor (2-amino-4,6-dichloro-*s*-triazine) to cobalt. If this exceeds 2,700 : 1 (by weight) the cobalt is completely removed as cobalt chloride and the catalyst is destroyed.

It is not clear at this stage why the particle alignment occurs. The nanotubes appear to grow preferentially through the aligned cobalt crystals. Overcrowding may be responsible for simultaneous tube growth from the surface. The experiment was conducted with the cobalt catalyst on the lower (inverted) silica surface. No aligned tube growth occurred when the cobalt-coated/etched surface was on the upper face, so that gravitational effects may well be significant.

An electron diffraction pattern (Fig. 4c) recorded for a group of nanotubes reveals a highly ordered graphitic arrangement within the bundles, especially with respect to the (001) plane. In addition, the outer rings indicate the presence of hexagonal graphite, commensurate with a preferential direction for nanotube growth (related to a non-helical arrangement corresponding to an armchair configuration). These patterns are usually observed (20–30%) within analysed samples.

While this work was in progress a report appeared describing the large-scale synthesis of aligned carbon nanotubes by passage of acetylene over iron nanoparticles embedded in mesoporous silica¹⁸. Pyrolytic formation of nanotubes in high yield that are substantially free from pyrolytic carbon overcoatings have been reported by Hyperion Inc.^{19,20}, but full details of the methods and product characterization have not been published, and the nanotubes do not appear to be aligned²¹. □

Received 13 March; accepted 12 May 1997.

1. Iijima, S. Helical microtubules of graphitic carbon. *Nature* **354**, 56–58 (1991).
2. Ebbesen, T. W. & Ajayan, P. M. Large scale synthesis of carbon nanotubes. *Nature* **358**, 220–222 (1992).
3. De Heer, W. A., Chatelain, A. & Ugarte, D. A carbon nanotube field-emission electron source. *Science* **270**, 1179–1180 (1995).
4. Terrones, M. et al. *Recent Advances in the Chemistry and Physics of Fullerenes and Related Materials Vol. 2* (eds Kadish, K. M. & Ruoff, R. S.) 599–620 (Electrochem. Soc., Pennington, NJ, 1995).
5. Dai, H. J., Wong, E. W. & Lieber, C. M. Probing electrical transport in nanomaterials: conductivity of individual carbon nanotubes. *Science* **272**, 523–526 (1996).
6. Ebbesen, T. W. et al. Electrical conductivity of individual carbon nanotubes. *Nature* **382**, 54–56 (1996).
7. Tans, S. J. et al. Individual single-wall carbon nanotubes as quantum wires. *Nature* **386**, 474–477 (1997).
8. Bockrath, M. et al. Single-electron transport in ropes of carbon nanotubes. *Science* **275**, 1922–1925 (1997).
9. Thess, A. et al. Crystalline ropes of metallic carbon nanotubes. *Science* **273**, 483–487 (1996).
10. Treacy, M. M. J., Ebbesen, T. W. & Gibson, J. M. Exceptionally high Young's modulus observed for individual nanotubes. *Nature* **381**, 678–680 (1996).
11. Amelinckx, S. et al. A formation mechanism for catalytically grown helix-shaped graphite nanotubes. *Science* **265**, 635–639 (1994).
12. Endo, M. et al. Pyrolytic carbon nanotubes from vapor-grown carbon fibres. *Carbon* **33**, 873–881 (1995).
13. Hsu, W. K. et al. Condensed-phase nanotubes. *Nature* **377**, 687 (1995).
14. Hsu, W. K. et al. Electrolytic formation of carbon nanostructures. *Chem. Phys. Lett.* **261**, 161–166 (1996).
15. Thurston, J. T. et al. Cyanuric chloride derivatives I. Aminochloro-s-triazines. *J. Am. Chem. Soc.* **73**, 2981–2983 (1951).
16. Chrisey, D. B. & Hubler, G. K. (eds) *Pulsed Laser Deposition of Thin Films* (Wiley, New York, 1994).
17. Terrones, M. et al. Pyrolytically grown B₃C₂N₃ nanomaterials: nanofibres and nanotubes. *Chem. Phys. Lett.* **257**, 576–582 (1996).
18. Li, W. Z. et al. Large synthesis of aligned carbon nanotubes. *Science* **274**, 1701–1703 (1996).
19. Tennent, H. G., Barber, J. J. & Hoch, R. US Patent No. 5578543 (1996).
20. Hausslein, R. W. Commercial manufacture and uses of carbon nanotubules. *187th Mtg of the Electrochem. Soc. (Abstr.)* 175 (Electrochem. Soc., Pennington, NJ, 1995).
21. Niu, C., Sichel, E. K., Hoch, R., Moy, D. & Tennent, H. High power electrochemical capacitors based on carbon nanotube electrodes. *Appl. Phys. Lett.* **70**, 1480–1482 (1997).

Acknowledgements. We thank J. Thorpe, D. P. Randall, S. Tehuacanero, R. Hernández, P. Mexia, R. Guardián and L. Rendón for providing electron microscope facilities, and D. Bernaerts for discussions. We thank CONACYT-México (M.T. and H.T.), the ORS scheme for scholarships (M.T. and W.K.H.), DGAPA-UNAM IN 107-296 (H.T.), EU-TMR grant (J.O.), the Royal Society (London) and the EPSRC for financial support.

Correspondence and requests for materials should be addressed to D.R.M.W. (e-mail: d.walton@sussex.ac.uk).

Chemical properties of element 106 (seaborgium)

M. Schädel*, **W. Brüche***, **R. Dressler†**, **B. Eichler†**,
H. W. Gäggeler†‡, **R. Günther§**, **K. E. Gregorich||**,
D. C. Hoffman||, **S. Hübener#**, **D. T. Jost†**, **J. V. Kratz§**,
W. Paulmann§, **D. Schumann***, **S. Timokhin***,
N. Trautmann§, **A. Türler†**, **G. Wirth*** & **A. Yakushev****

* *Gesellschaft für Schwerionenforschung, 64291 Darmstadt, Germany*

† *Labor für Radio- und Umweltchemie, Paul Scherrer Institut, 5232 Villigen, Switzerland*

‡ *Department für Chemie und Biochemie, Universität Bern, 3012 Bern, Switzerland*

§ *Institut für Kernchemie, Universität Mainz, 55099 Mainz, Germany*

|| *Lawrence Berkeley National Laboratory, Berkeley, California 94720, USA*

¶ *Glenn T. Seaborg Institute for Transactinium Science, Livermore, California 94551, USA*

Institut für Radiochemie, Forschungszentrum Rossendorf, 01314 Dresden, Germany

∗ *Institut für Analytische Chemie, Technische Universität Dresden,*

01062 Dresden, Germany

** *Flerov Laboratory of Nuclear Reactions, Joint Institute of Nuclear Research, Dubna, Russia*

The synthesis, via nuclear fusion reactions, of elements heavier than the actinides, allows one to probe the limits of the periodic table as a means of classifying the elements. In particular, deviations in the periodicity of chemical properties for the heaviest elements are predicted as a consequence of increasingly strong relativistic effects on the electronic shell structure^{1–7}. The trans-

actinide elements have now been extended up to element 112 (ref. 8), but the chemical properties have been investigated only for the first two of the transactinide elements, 104 and 105 (refs 9–19). Those studies showed that relativistic effect render these two elements chemically different from their lighter homologues in the same columns of the periodic table (Fig. 1). Here we report the chemical separation of element 106 (seaborgium, Sg) and investigations of its chemical behaviour in the gas phase and in aqueous solution. The methods that we use are able to probe the reactivity of individual atoms, and based on the detection of just seven atoms of seaborgium we find that it exhibits properties characteristic of the group 6 homologues molybdenum and tungsten. Thus seaborgium appears to restore the trends of the periodic table disrupted by relativistic effects in elements 104 and 105.

Calculations of the electron configurations of heavy atoms^{1–5} have predicted that sudden changes in the structure of the electron shells may appear due to strongly increasing relativistic effects. These relativistic effects are proportional to the square of the nuclear charge, which attracts electrons in spherically symmetric orbitals (*s* and *p*_{1/2}) most strongly to the nucleus. This, in turn, means that the nuclear charge is more efficiently screened, thus allowing expansion of the non-spherical *d* and *f* orbitals. Because the chemical behaviour of an element is strongly dependent on the electronic configuration, such relativistic effects can lead to unexpected chemical properties^{6,7}.

Studies of the chemical properties of elements 104 (rutherfordium, Rf) and 105 (hahnium, Ha; the name dubnium has also been proposed, but has yet to be approved by the International Union of Pure and Applied Chemistry) were full of surprises^{18,19}. The non-tantalum-like behaviour of hahnium in aqueous solution^{10,11,20}, for example, and its similarity to niobium and/or protactinium, depending on its chemical environment, demonstrated that the chemical properties cannot be reliably extrapolated from the trends observed in its lighter homologues. Such surprises have also been seen in thermo-chromatographic^{9,21} and gas-chromatographic experiments^{12,13,15,16}. Therefore, it is of interest to investigate whether the chemical properties of element 106 (seaborgium, Sg) resemble those of the lighter homologues in group 6 (molybdenum and tungsten) or those of the pseudo-group-6 element uranium.

We synthesized the most neutron-rich seaborgium isotopes^{22,23}, ²⁶⁵Sg and ²⁶⁶Sg, in a nuclear fusion reaction between ²²Ne ions from the GSI UNILAC accelerator and a ²⁴⁸Cm target with a rate of the order of one atom per hour (ref. 24). The ²⁶⁵Sg and ²⁶⁶Sg nuclei were knocked out of the target foil and were stopped in helium gas loaded with tiny (0.1–1 μm) solid particles (aerosols). Within about three seconds, the helium transported the reaction products—attached to aerosols—along capillary tubes to two different sets of chemical devices. To provide conclusive evidence that a seaborgium atom had passed through the chemical separation procedures, the experiments were designed to detect the characteristic α-decay chains of the isotope ²⁶⁵Sg, and the corresponding daughter nuclides ²⁶¹Rf and ²⁵⁷No (ref. 24). In addition, fission fragments were measured from spontaneous fission decay, which would arise from ²⁶²Rf, the α-decay product of ²⁶⁶Sg. An earlier attempt to perform a chemical separation of element 106 fell short of unambiguously showing that the observed, by itself unspecific, spontaneous fission decay originated from an isotope of element 106 (ref. 25). We have applied two chemical separation techniques, one probing the formation of volatile oxychlorides in a gas-chromatographic experiment, and another one probing the formation of oxo- or oxyfluoride complexes in aqueous solution by liquid chromatography.

In classical gas chromatography, a substance under investigation is introduced into a flowing stream, and the time taken for the sample to emerge from chromatographic system is measured. In our experiment, in contrast, the nuclear reaction products were continuously supplied and separated in OLGA III—the on-line gas chemistry apparatus¹⁷. This technique uses the half-life of the